Ultramicroscopy 171 (2016) 8–18

Contents lists available at ScienceDirect

Ultramicroscopy

journal homepage: www.elsevier.com/locate/ultramic

Electron beam dynamics in an ultrafast transmission electron microscope with Wehnelt electrode

K. Bücker [a,1], M. Picher [a,1], O. Crégut [a], T. LaGrange [b], B.W. Reed [c], S.T. Park [c], D.J. Masiel [c], F. Banhart [a,*]

[a] Institut de Physique et Chimie des Matériaux de Strasbourg, UMR 7504 CNRS, Université de Strasbourg, 23 rue du Loess, 67034 Strasbourg, France
[b] Interdisciplinary Centre for Electron Microscopy, École Polytechnique Fédérale de Lausanne, 1015 Lausanne, Switzerland
[c] Integrated Dynamic Electron Solutions, Inc., 5653 Stoneridge Drive 117, Pleasanton, CA 94588, USA

ARTICLE INFO

Article history:
Received 9 May 2016
Received in revised form
18 July 2016
Accepted 18 August 2016
Available online 20 August 2016

Keywords:
Ultrafast transmission electron microscopy
Dynamic transmission electron microscopy

ABSTRACT

High temporal resolution transmission electron microscopy techniques have shown significant progress in recent years. Using photoelectron pulses induced by ultrashort laser pulses on the cathode, these methods can probe ultrafast materials processes and have revealed numerous dynamic phenomena at the nanoscale. Most recently, the technique has been implemented in standard thermionic electron microscopes that provide a flexible platform for studying material's dynamics over a wide range of spatial and temporal scales. In this study, the electron pulses in such an ultrafast transmission electron microscope are characterized in detail. The microscope is based on a thermionic gun with a Wehnelt electrode and is operated in a stroboscopic photoelectron mode. It is shown that the Wehnelt bias has a decisive influence on the temporal and energy spread of the picosecond electron pulses. Depending on the shape of the cathode and the cathode-Wehnelt distance, different emission patterns with different pulse parameters are obtained. The energy spread of the pulses is determined by space charge and Boersch effects, given by the number of electrons in a pulse. However, filtering effects due to the chromatic aberrations of the Wehnelt electrode allow the extraction of pulses with narrow energy spreads. The temporal spread is governed by electron trajectories of different length and in different electrostatic potentials. High temporal resolution is obtained by excluding shank emission from the cathode and aberration-induced halos in the emission pattern. By varying the cathode-Wehnelt gap, the Wehnelt bias, and the number of photoelectrons in a pulse, tradeoffs between energy and temporal resolution as well as beam intensity can be made as needed for experiments. Based on the characterization of the electron pulses, the optimal conditions for the operation of ultrafast TEMs with thermionic gun assembly are elaborated.

1. Introduction

Transmission electron microscopy (TEM) with ultrashort electron pulses has become a most powerful tool in the past years to study dynamic phenomena at the nanoscale [1–6]. Ultrafast or dynamic transmission electron microscopes (UTEM, DTEM) combining high temporal with high spatial resolution appear to be the highly capable instruments for gaining insight into ultrafast processes at the nanometer scale. In the past decade, much effort has been devoted to the technical development of ultrafast electron microscopy and to push the limits of spatial and temporal resolution [7–13]. Two instrumental approaches have been developed so far. The first is based on field emission electron guns capable of photoemission via excitation with a femtosecond laser pulse, and often assisted by the extraction field of the first anode. The other approach is a thermionic electron emitter that works with a Wehnelt electrode around the cathode to focus the electrons to a small virtual source at its focal point, the so-called gun cross-over. While the field emission setup has hitherto been mainly used for stroboscopic experiments [14], the thermionic gun has been applied to work in both the stroboscopic and the single-shot mode [2,11,15].

In conventional TEMs, the electrons in the continuous nanoampere beam normally do not interact with each other, i.e., they are spread far apart in space and there is typically only one electron propagating down the column every couple of nanoseconds. In contrast, the compression of many electrons into a picosecond pulse having an effective peak current on the order milliamperes with small spatial and temporal volume leads to mutual repulsion.

* Corresponding author.
E-mail address: florian.banhart@ipcms.unistra.fr (F. Banhart).
[1] These authors have contributed equally to this work.

http://dx.doi.org/10.1016/j.ultramic.2016.08.014
0304-3991/

Nonlinear and stochastic spatial broadening of the electron pulse in the plane normal to the beam can cause a loss of coherence in imaging while the elongation of the pulse in the beam direction leads to a lengthening in time. Mutual repulsion of electrons due to space charge may also lead to a considerable energy spread. Space charge around the cathode and mutual repulsion in small cross-overs (Boersch effect) is detrimental in TEM with short electron pulses and therefore limits the spatial and temporal resolution in microscopy as well as the energy resolution in EELS.

In stroboscopic experiments, where the specimen recovers after each excitation within a short time, these limits can, in principle, be overcome if the pulses contain one or a few electrons [6]. However, the "single-electron" mode has its restrictions. The interval between two pulses needs to be longer than the recovery time of the specimen, thus limiting the repetition frequency of laser excitation. On the other hand, the number of electrons to produce an image of sufficient signal-to-noise ratio [7] needs a minimum number of repetitions. Satisfying these two requirements by long exposure times is often in conflict with inevitable instrumental instabilities such as specimen drift. It is therefore, for most experiments under realistic conditions, necessary to work with a larger number of electrons per pulse while minimizing space charge effects by careful optimization of the emission parameters. Compromises among temporal resolution, energy resolution, spatial resolution, and intensity of the beam have to be found for multi-purpose applications.

The optimization of the spatial and temporal resolution as well as the energy width of the beam requires a detailed understanding of the electron dynamics in the microscope. This demands detailed knowledge of the electron beam path, how the electrons interact with each other, and how these interactions lead to broadening effects. Knowing the changes in the electron beam path and time of flight in the low-energy regime during acceleration under different gun settings and geometries is crucial since electrons on different trajectories do not necessarily arrive at the same time on the specimen. Several studies have already been undertaken in the past to characterize electron pulses in thermionic guns [7,11–13,16,17]. Field emission guns, with their sharp tips, small emission area and surface field enhancement, have shown advantages when high coherence is required [14]. Due to the small emission area, such an operation is limited to the quasi-single-electron mode. Thermal electron guns, on the other hand, are less complex, inexpensive, and easier to use and maintain, and allow for a high degree of flexibility in the emission characteristics when the Wehnelt bias voltage can be independently adjusted. Easily exchangeable cathodes with large emission area can be used so that the pulses contain a large number of electrons. These conditions are more appropriate for investigations (especially in materials science) that require short exposure times to limit the effects of microscope instabilities on the resolution. Furthermore, the combination of stroboscopic and single-shot operation in one microscope requires a versatile gun assembly, i.e., the use of different cathodes and adjustable electric fields around the emitter to control different space charge distributions.

Optimizing such a gun setup with an adjustable Wehnelt bias is the subject of the present study. It is shown experimentally how the Wehnelt bias, the geometry of the cathode, and the intensity of the UV laser pulses on the cathode influence the duration and the energy spread of picosecond electron pulses. It is found that electron trajectories in the low-energy regime (before acceleration) play the major role in determining the duration of the pulses and as such the temporal resolution of the microscope. The beam current density (along the beam propagation), on the other hand, has an influence on the energy distribution in a pulse via repulsion effects. The influence of Wehnelt aberrations on the emission characteristics is studied in detail. The high flexibility of the thermionic gun with an adjustable potential Wehnelt electrode allows trade-offs between spatial, temporal, and energy resolution and appears to be the most suitable solution for the study of ultrafast phenomena in materials. The study was carried out with one of the first commercial UTEMs and should, hence, be of importance for the further development of the technique for a wide range of users and applications.

2. Experimental procedure

The electron microscope of the present study is based on a JEOL 2100 TEM with a thermionic gun and was modified by IDES, Inc. to operate in the pulsed photoelectron mode [11,18]. The microscope modifications provide UV laser access to the photocathode for photoelectron pulse generation and IR laser access to the specimen to optically drive transient states in materials. The optical periphery including the laser is attached to the microscope on two optical tables that are supported by the anti-vibration system of the microscope. This gives the whole setup a high mechanical stability and avoids shifts of the laser beam relative to the microscope. Two flat mirrors are used to direct the IR drive laser onto the specimen and the UV laser onto the cathode (Fig. 1). The mirror for the drive laser is located on top of the objective pole piece whereas the UV mirror is in an added drift section on top of the condenser. An additional electron lens (C0) [19] below the anode is used to collect electrons from a larger angle and so to increase the electron beam current and to focus the electrons through the hole in the UV mirror into the condenser. The electron pulses are recorded with a CCD camera (Gatan Ultrascan, 2 k x k pixels) or an electron energy-loss spectrometer (Gatan Enfinium). For the experiments shown below, an infrared fiber laser (1030 nm) with 350 fs pulses and an average power of up to 10 W is used that can be operated at different repetition frequencies varying from 250 kHz to 40 MHz. The IR beam is split into two beams, one which is frequency-quadrupled to 258 nm and such that both IR and UV pulses are emitted simultaneously. An optical delay line (0–3 ns) with a movable mirror in the IR beam, controlled by the imaging software (Gatan Digital Micrograph), is used to generate the delay between the optical pump on the specimen and the electron probe.

The electron gun is a conventional thermionic emitter with Wehnelt electrode. To obtain a low energy spread of the photoelectrons, tantalum emitters were used that have a work function

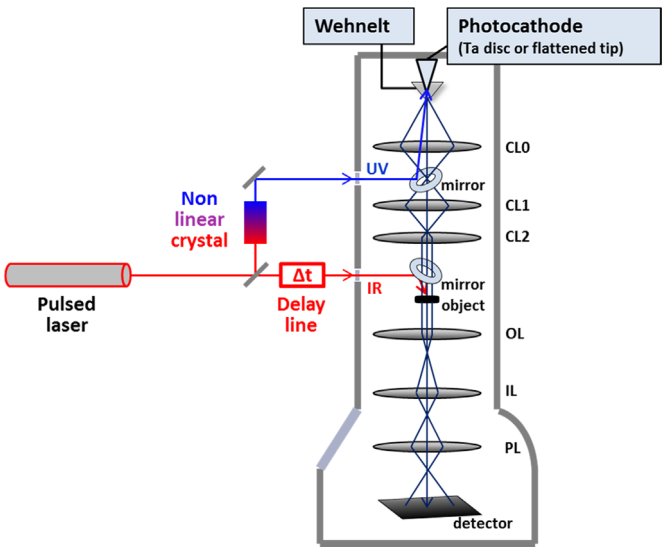

Fig. 1. Simplified schematic drawing of the ultrafast TEM.

(4.2 eV) slightly below the photon energy (4.8 eV). Temperature, crystal facet and surface contamination affect the work function and quantum efficiency of cathode materials [24]. Thus, to prevent from progressive deterioration, the cathode was regularly flashed by heating which removes contaminants and oxides. In addition, considering the size of the UV beam (diameter of ~100 μm) hitting the polycrystalline cathodes, one can consider that the differing work functions associated crystal orientation are averaged to a value of 4.2 eV. The beam characteristics were measured with Ta discs (diameter 900 μm) and Ta tips (cones with 90° angle and flattened tip of 16 μm diameter).

The spatial resolution of the microscope in the photoelectron mode with a Ta disc as emitter is shown in Fig. 2a. A gold crystal was imaged with photoelectrons in the stroboscopic mode without a drive laser on the specimen. The UV intensity was 15 mW and the repetition frequency 2 MHz. The exposure time of the image was 10 s, thus integrating 2×10^7 exposures. The (111) lattice fringes with a spacing of 0.23 nm are clearly visible (even the reflections of the (002) planes with interplanar spacing of 0.20 nm are weakly visible in the FFT). An EEL spectrum taken with very low UV intensity is shown in Fig. 2c. The width of the zero-loss photoelectron peak is 0.79 eV (FWHM) which is close to the theoretical limit of 0.6 eV, given by the difference between the UV photon energy and the work function of the Ta emitter.

The synchronization of the IR pulses and the electron pulses on the specimen was achieved by using the PINEM effect (Photon-Induced Near-field Electron Microscopy) [16,17,20], in which the overlap of the photoelectron pulses with the optical pump pulses are observed via the inelastic electron-photon scattering in the photonic near field of the specimen. The effect is observed in the stroboscopic mode and makes use of the energy gain or loss of electrons when they pass next to the specimen surface (aloof spectroscopy). The zero-loss peak in the EEL spectrum shows side peaks with an energy shift associated with the optical pump photon energy, $\Delta E = n\ \mathrm{h}\ \nu$, where n is an integer, h is the Planck's constant and ν the frequency of the IR photons (Fig. 3). At time zero ($t=0$), i.e., when the photon and electron pulses arrive at the same time, the maximum intensity is scattered from the central zero-loss peak into the side bands. By moving the mirror of the delay line and taking PINEM spectra at different mirror positions, a temporal scan over the electron pulse can be taken. The ratio between the unscattered intensity in the central peak and the scattered intensity in the side peaks can be used to probe the electron distribution in a pulse along the beam direction [16,17]. The width of the peak reflects the temporal width of the electron pulses and thus the temporal resolution of the measurement.

3. Results

3.1. Emission characteristics of the electron gun

The intensity, temporal behavior, and energy spread of the electron pulses were measured as a function of UV laser intensity, Wehnelt bias, and distance between cathode and Wehnelt aperture. The measurements were taken with a Ta disc and a Ta cone emitter, both at cathode-Wehnelt gaps of 550 μm and 760 μm. The bias could not be directly measured and was estimated from electrical circuit diagrams and calibration curves provided by the microscope manufacturer. For the measurement of parameters where the mutual repulsion of electrons occurs, a high and constant UV laser intensity was used. The data were acquired at $\lambda = 258$ nm, repetition rate of 500 kHz, pulse duration of 370 fs, and an average laser power of 1 mW, corresponding to 2 nJ per pulse. It has to be stressed that these conditions aim at measuring the pulse characteristics in the intense regime, contrary to the "single-electron" mode.

Fig. 4a shows the evolution of the electron emission pattern from a Ta *disc* (imaging with focused C2 lens) as a function of Wehnelt bias. The pulsed photoelectron mode behaves in a similar way as the thermionic mode [21]. The central spot slightly shrinks when the bias increases until a small halo shows up (Fig. 4a-4). If the bias is further increased, the small halo progressively converges until it merges with the central spot. A particular case, presented in Fig. 4b, appears when a tantalum *tip* is used at short cathode-Wehnelt distances (550 μm). Electrons emitted from the side walls of the tantalum cone (shank emission) appear as a large ring that converges with increasing bias.

Fig. 4c shows the evolution of the beam current as a function of Wehnelt bias for both cathodes and for two cathode-Wehnelt distances. The beam current was measured on the viewing screen of the microscope. This is a relative value for the throughput because the beam current leaving the gun is higher than the current arriving on the viewing screen due to the loss of electrons at apertures in the column. Due to the increasing lens strength of the Wehnelt, which causes the beam to expand more rapidly after crossover, the beam intensity decreases as the bias increases. After reaching a minimal value, the current raises again at high bias before it vanishes. The peak at high bias is correlated with the appearance of the small halo in the emission pattern (Figs. 4a-4, b-4).

The small halo, appearing with all cathodes and at all cathode-Wehnelt gaps (Figs. 4a-4, b-4), is most likely due to the spherical aberration of the Wehnelt, acting as a poor lens when the bias is

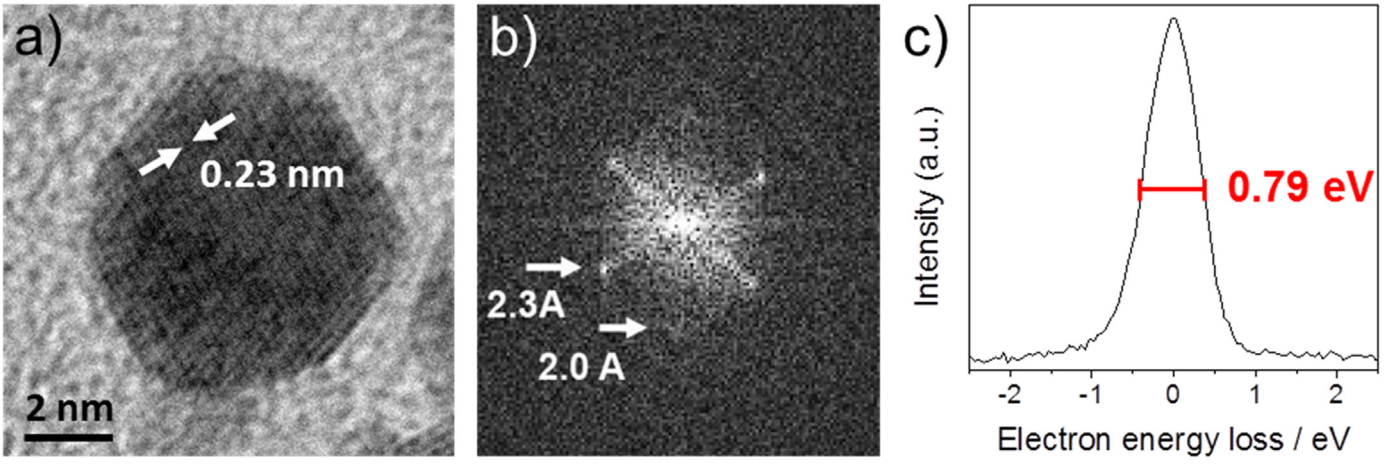

Fig. 2. Resolution in the photoelectron mode without laser illumination of the specimen. (a) Lattice image of a gold crystal on amorphous carbon; (b) Fourier transform of the lattice image; (c) zero-loss peak of the EEL spectrum at low intensity conditions.

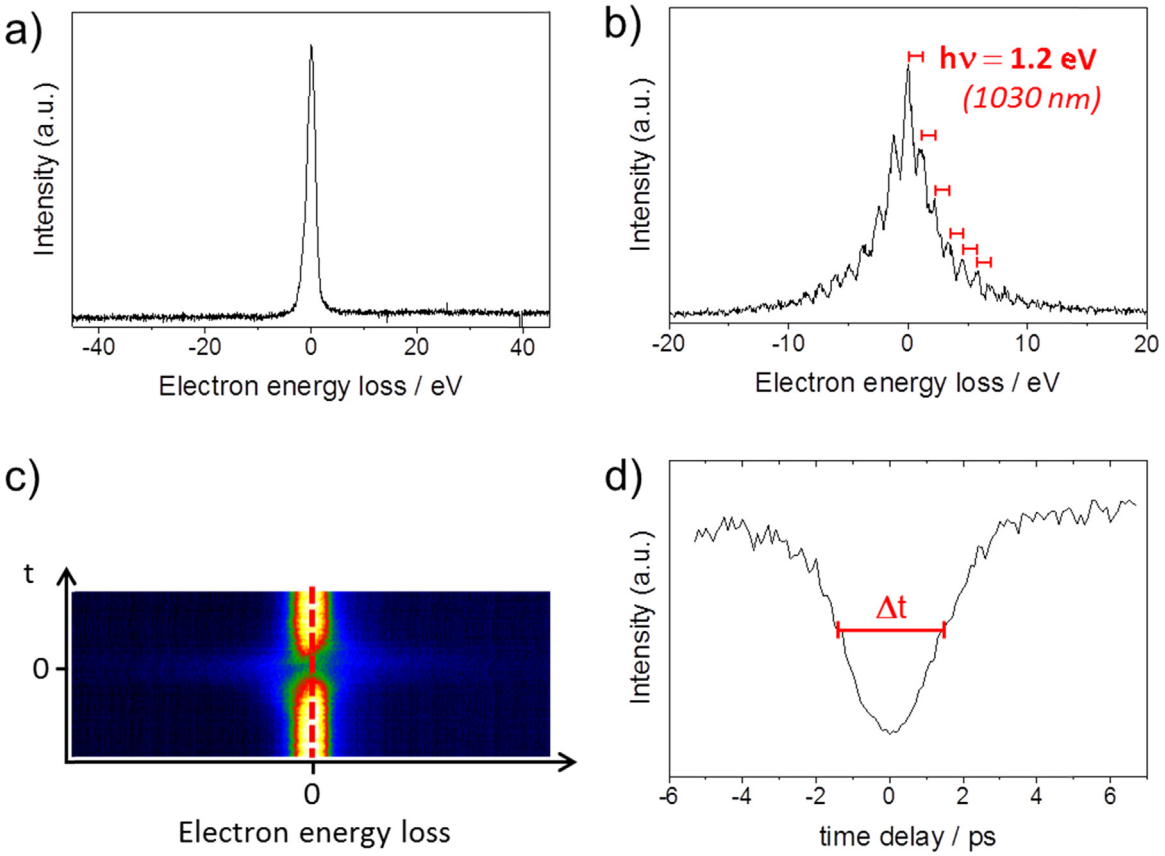

Fig. 3. PINEM (Photon-Induced Near-Field Electron Microscopy) spectra and measurement of temporal resolution using Ag nanowires. (a) Zero-loss peak of the EELS; (b) zero-loss with the PINEM spectrum; (c) time scan over the zero-loss EELS (the PINEM effect is visible at t=0 as the weak horizontal blue line); (d) profile of the time scan at E=0 (dashed line in (c); the width Δt of the dip at FWHM is indicated. (For interpretation of the references to color in this figure legend, the reader is referred to the web version of this article.)

high and the focal length correspondingly short. At lower bias, the throughput decreases with increasing bias (Fig. 4c) because the beam is expanded below the Wehnelt cross-over and increasingly blocked by the anode aperture. At higher bias, however, the cross-over is closer to the Wehnelt and the beam is focused again by the Wehnelt field before entering the anode stack, resulting in a focused or collimated beam at the anode aperture. This leads to a new rise in beam current (halo) that results from the Wehnelt aberration. Finally, at even higher bias, the emission vanishes when the extraction field on the cathode crosses zero and reverses its direction, and emitted electrons are pushed back into the cathode.

Shank emission from the sloped side walls of the *conical tip* appears at low bias (large ring in Fig. 4b-1 and b-2) and is due to the fact that the laser spot (100 μm) is much larger than the flattened area of the tip (16 μm). Shank emission dominates at low bias, as shown in Fig. 4d, but vanishes towards larger bias where the ring merges with the central spot. The spot formed by the on-axis electrons is weak at low bias but slightly increases in intensity with increasing bias. A maximum is reached at intermediate bias, followed by a larger maximum where the aberration-induced halo appears. At minimum bias, the emission region on the filament is generally large and electrons are emitted from outside the center of the cathode. As in thermal emission from a tip, the large shank emission ring converges with increasing bias until all of the electrons that emerge from the accelerator are emitted from the flattened tip of the cathode only. The large ring is due to the local electric field at the side walls, which acts in such a way that only electrons at a certain distance from the tip are transmitted [22].

By counting the electrons that arrive on the CCD camera, a highest average photoelectron current of 625 pA was measured at a UV power of 2 nJ/pulse, zero bias (high extraction field on the cathode), a Ta tip at 550 μm from the Wehnelt, and combining shank with on-axis emission. At a repetition rate of 500 kHz, this corresponds to about 8000 electrons per pulse on the camera. However, the number of electrons generated at the photocathode is higher since some electrons are blocked by fixed apertures in the accelerator. Based on our estimation that 7×10^4 photoelectrons are produced per laser pulse (c.f. discussion section), we obtain an average current of 6 nA in the gun; therefore roughly 10% of all emitted electrons reach the camera. Depending on the cathode-Wehnelt distance and the bias, the throughput could also be higher under optimum conditions.

3.2. Temporal resolution

The arrival time of the electrons on the specimen is shown in Fig. 5a. Here, the reference of zero shift is defined at minimum bias of 80 V for each cathode type and Wehnelt gap. As expected, the electrons are retarded with increasing bias due to the negative potential of the Wehnelt. The shift is more pronounced for large cathode-Wehnelt gaps. Fig. 5b and c show the temporal shifts measured separately for the central spot (on-axis electrons) and the small high-bias halo as well as the low-bias shank emission from the tip. Interestingly, electrons from the different emission regions arrive at different times. A difference of about 100 ps is measured between the central spot and the small aberration-induced halo (Fig. 5b, red circles). A likely interpretation is that the small halo comprises electrons having trajectories far from the optical axis. Furthermore, the surface extraction field on the

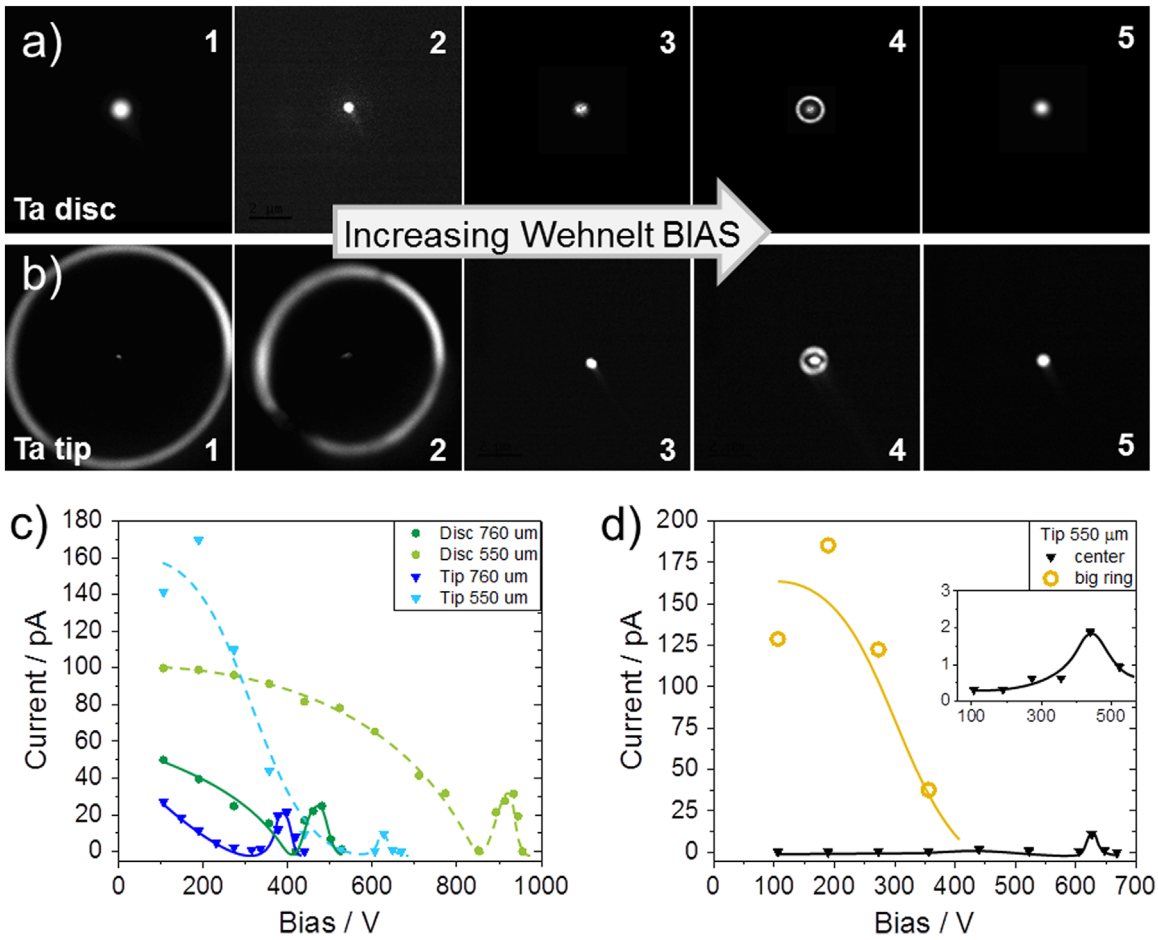

Fig. 4. (a) Emission pattern as a function of Wehnelt bias for the Ta disc at 550 µm from the Wehnelt. (b) Ta tip at 550 µm from the Wehnelt. (c) Total beam current as a function of Wehnelt bias for the two cathodes and for two different cathode-Wehnelt gaps. (d) Individual beam current measured for the large shank emission ring and the central spot (Fig. 4b) separately using the Ta tip at 550 µm from the Wehnelt. The inset shows the central beam current on a smaller scale.

cathode decreases faster for off-axis emission. Electrons emitted at larger angles are not collected at low bias because the focusing by the Wehnelt is not strong enough for transmission. For shank emission (large ring), an initial delay of approximately 17 ps relative to on-axis electrons is measured at low bias (Fig. 5c, upper curve). At 400 V, i.e., where the ring merges with the central spot, a uniform time zero is obtained. This can be understood if the Wehnelt bias, on one hand, retards the electrons due to the additional potential barrier but, on the other hand, moves the emission circle towards the tip, changing the trajectories. This would reduce the path length and consequently shorten the time of flight.

Fig. 5d shows the temporal width Δt of the pulses as a function of the bias. Both halo and shank emission ring are excluded so that only the central beam contributes. Here, the temporal width was measured from tail to tail of the PINEM scan (c.f., Fig. 3d) with a full width at 5% of the maximum. The full width half maximum (FWHM) measurement was not applicable for pulses with broad ΔE and/or long Δt since in these two cases, the PINEM signal affects only a small fraction of the total intensity of the zero loss peak. Thus, this measurement at full width at 5% maximum is more suitable for comparing all of the data in a consistent way. The shortest pulses reported here have a 4.5 ps duration at 5% maximum, corresponding to 1.9 ps FWHM which would be the temporal resolution of the microscope in the regime of many electrons per pulse (in the quasi-single-electron mode, the temporal width can be smaller).

Generally, an increase of the bias leads to a temporal broadening of the pulses. Two contributions to the temporal spread have to be considered. The first is the influence of the extraction field on the cathode which is important for all emitted electrons, be it on-axis propagation or electrons from the halos. At low bias, the extraction field is high and the acceleration of the pulse correspondingly rapid, leading to a small temporal spread. With increasing bias and decreasing longitudinal field, the extraction is less efficient, leading to temporal broadening. At zero field on the cathode, the extraction time (t_0) as well as the temporal width go towards infinity (this is a simplified model because it only considers the longitudinal and not the transverse direction which also reduces the extraction field closer to the Wehnelt). This behavior is seen in Fig. 5d. At the same time, however, the transmission goes to zero, making this high-bias regime unsuitable for time-resolved experiments.

The larger contribution to the temporal spread in the high-bias regime (before the emission vanishes) stems from the halo having different arrival time (Fig. 5b). Whereas at low bias, where no halo appears in the emission pattern, the temporal broadening does not exceed a few picoseconds, the pulses may lengthen to up to 100 ps when the aberration-induced halo appears at higher bias and contributes to the beam (corresponding to the difference Δt between central beam and halo in Fig. 5b). Thus, a major contribution to the temporal broadening at high bias can be due to the halo (provided that it is not blocked by the anode aperture), stemming from the transmission of off-axis electrons with longer trajectories and thus different arrival times. Though there is a significant increase of the total beam current at high bias due to contribution of electrons from the small halo, it results in a considerable loss of

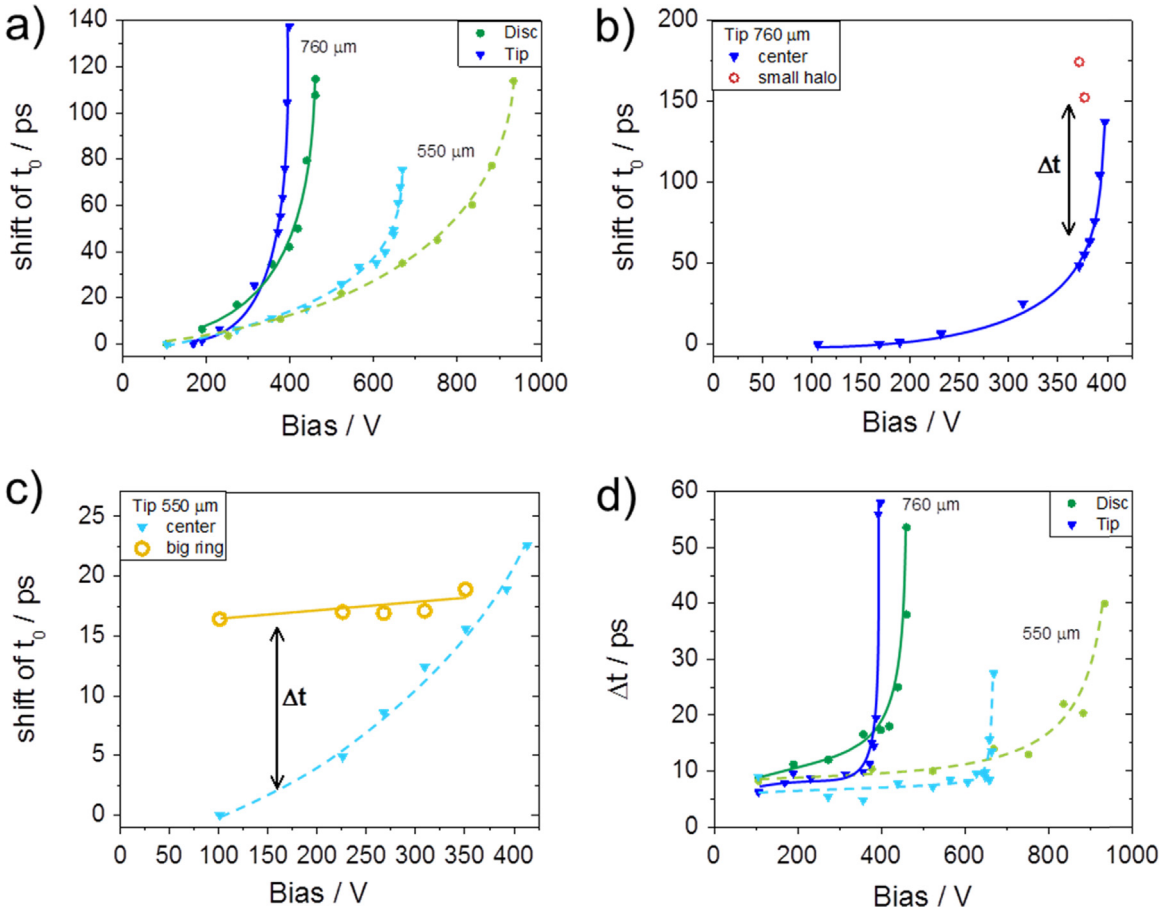

Fig. 5. (a) Arrival time t_0 of electron pulses as a function of Wehnelt bias for the two cathodes and two different cathode-Wehnelt gaps. (b) Shift of t_0 for the Ta tip at 760 µm distance to the Wehnelt, measured separately for the small aberration-induced halo and the central spot (shank emission excluded). (c) Comparison of shank emission (large ring) with central beam for the Ta tip at 550 µm distance. (d) Temporal width of the electron pulses as a function of Wehnelt bias. Only the central beam (on-axis) contributes; all halos are excluded. (For interpretation of the references to color in this figure legend, the reader is referred to the web version of this article.)

temporal resolution. Nevertheless, even when the halo is excluded, the temporal spread of the central beam increases with bias. At maximum bias, where the halo merges with the central beam, a separation between the two distributions of electrons is not possible, and the temporal width appears to strive to infinity. These data clearly show that the Wehnelt bias provides a controlled means for making trade-offs between signal and temporal resolution.

The variance in electron arrival times within the pulse is also evident in the PINEM signal as shown in Fig. 6. Both central spot and small halo contribute to the beam at higher bias (shank emission is excluded). Time-scans over the zero-loss EELS obtained at various bias values are shown for the emission from the tip at 550 µm Wehnelt gap (this corresponds to the light blue curve in Fig. 5d). Here, the bias has been finely tuned in order to probe the electron pulse at the threshold bias where the small halo is visible in the filament image. In Fig. 6a, acquired at a bias of 660 V (c.f., Fig. 3c), one can clearly separate two broadened regions (indicated by arrows) in the PINEM scan, corresponding to two electron pulses with different arrival times. Below the threshold bias, where only on-axis electrons contribute (left peak), the pulse is short, though the bias influences the arrival time. As the bias increases, the pulse is progressively retarded and broadened due to the decreasing extraction field on the cathode. However, when off-axis electrons contribute (right peak), the PINEM signal exhibits a long and delayed pulse. As the bias is further increased, these two pulses merge to form an extended pulse with duration of tens of picoseconds.

Another hypothesis to explain temporal broadening would be a wide distribution in electron energies, leading to different times of flight. In a simple acceleration-propagation model, the electron trajectory can be divided into linear acceleration (between cathode and anode) and field-free drift (below the anode). For both, an analytical estimation of the temporal spread due to the initial energy spread can be derived. The space charge effect increases the temporal spread during the flight, in particular during the acceleration. However, we can only measure the final temporal spread at the specimen.

An approximate expression [9] for the temporal spread Δt in the acceleration regime is given by:

$$\Delta t \approx \frac{d}{eV}\frac{\Delta E}{v_i}$$

where d is the distance between cathode and anode, e the elementary charge, V the acceleration voltage, v_i the initial velocity, ΔE the (constant) energy spread, such that V/d represents the acceleration field. Taking the initial energy spread of 0.6 eV (by setting $<E_i>=0.3$ eV and $\Delta E_i=0.6$ eV), we obtain a temporal spread $\Delta t=1.8$ ps at 1×10^6 V/m, and 0.6 ps at 3×10^6 V/m. However, assuming the largest measured initial energy spread of $\Delta E_{max}=200$ eV (v_i remains at 3×10^5 m/s), as shown in Fig. 7, this would result in a temporal spread of more than $\Delta t=400$ ps. The latter is far above the largest measured temporal spreads (Figs. 5d, 8). Therefore, it can be deduced that the temporal spread in the acceleration is dominated by the initial energy spread (where v_i is the smallest). Space charge induced effects, which are responsible

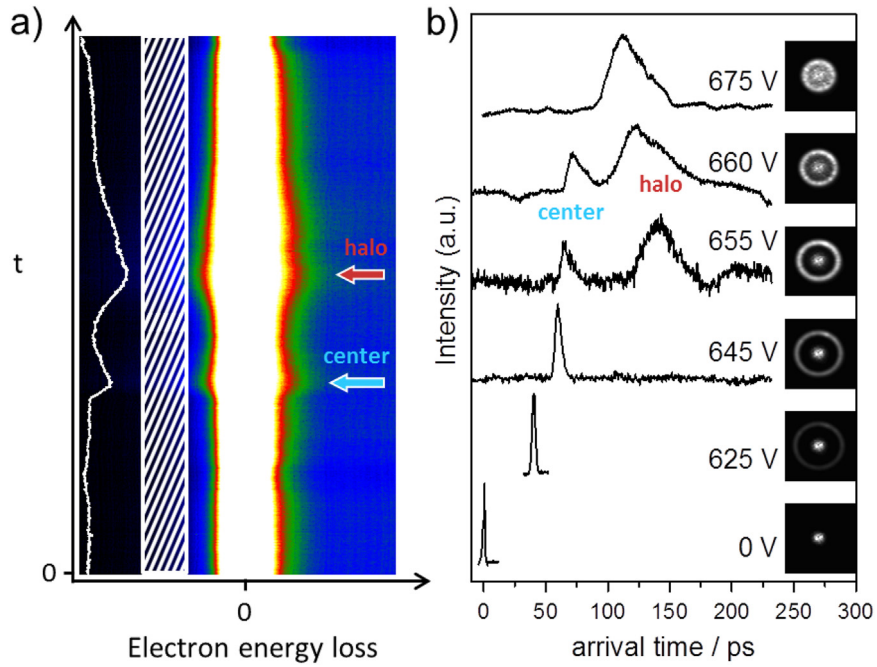

Fig. 6. (a) Time scan over the zero-loss EELS at Wehnelt bias of 660 V. The tip at 550 μm gap was used. The PINEM effect is visible at two different delays, corresponding to on-axis and halo electrons, respectively. In the left inset (white curve on black background), the time-scan profile measured at E = 13 ± 3.5 eV (white dashed rectangle) is shown. (b) Time-scan profiles acquired at different bias. The temporal shift and broadening can be seen for the central beam and halo separately.

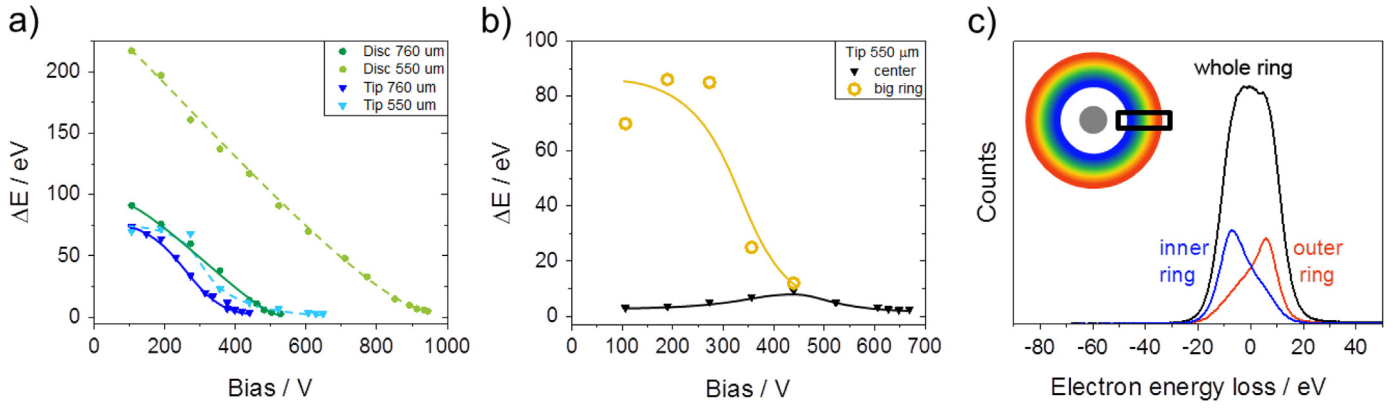

Fig. 7. (a) Energy spread of the electron pulses as a function of Wehnelt bias for two cathodes and for two different cathode-Wehnelt gaps. (b) Separation of ring and central spot for the Ta tip at 550 μm distance. (c) Energy distribution within the ring, evidencing the strong chromatic aberration of the Wehnelt at 550 μm and 80 V. The rainbow scheme indicates the energy distribution of electrons within the ring. The inner ring (red) corresponds to higher energy while lower energy electrons correspond to the outer ring (blue). (For interpretation of the references to color in this figure legend, the reader is referred to the web version of this article.)

for the large observed energy broadening, occur later during the propagation.

The temporal spread in the field-free propagation regime is given by

$$\Delta t = \frac{t}{\beta^2\gamma^3}\frac{\Delta E}{m_0c^2}$$

where t is the average travel time of the electrons between gun and specimen, $\beta = v/c = 0.69$, $\gamma = 1.39$ (Lorentz factor), and $m_0c^2 = 511$ keV. By assuming the highest observed energy spread of $\Delta E = 200$ eV and $t = 3.8$ ns, we obtain a temporal spread of only $\Delta t = 1.1$ ps.

The experimentally determined energy (due to space charge induced effects) and temporal spreads are shown in Fig. 8. The energy spread decreases as the bias increases (see also Fig. 7a) whereas the temporal spread shows the opposite behavior. It is therefore reasonable to assume that the observed temporal spread does not dominate the observed energy spread. In other words, the contribution of space charge effects to the temporal spread is negligible or very small for the number of electrons per pulse measured here ($\sim 10^4$).

Taking the initial energy spread of 0.6 eV, we can tentatively add the contributions of $\Delta t = 1.3$ ps in the acceleration regime, the UV pulse duration of 370 fs, and a possible temporal spread in the field-free propagation regime which is always below 1.5 ps. We arrive at a total temporal spread of the order 3 ps which is close to the smallest measured temporal spread in the low bias domain (2.5 ps FWHM). Furthermore, the temporal spread in the acceleration regime strongly depends on the field strength via the Wehnelt bias. We can conclude that space charge gives only a minor contribution to the temporal spread attained under optimal Wehnelt bias settings.

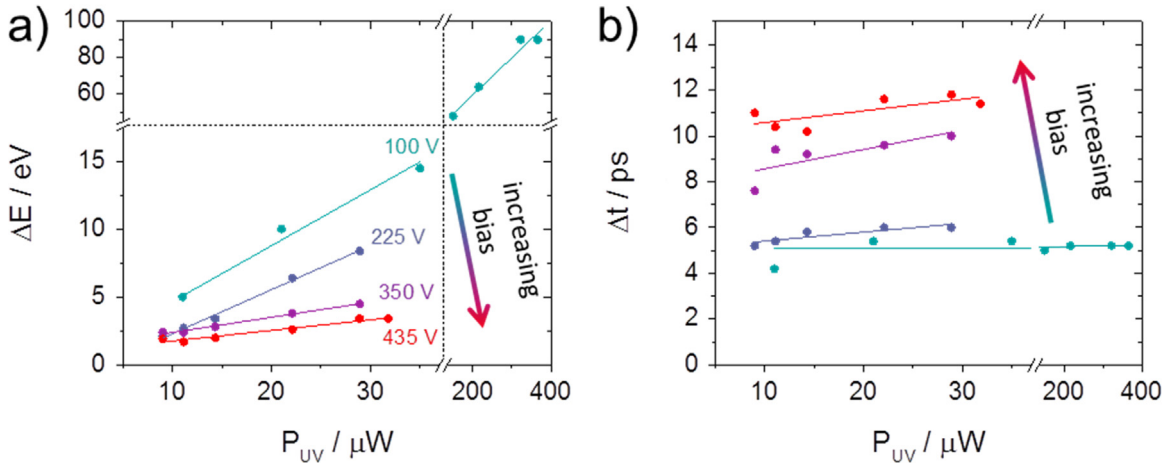

Fig. 8. Energy (a) and temporal (b) widths of the electron pulses as a function of UV power on the cathode. Data acquired at different Wehnelt bias by using the Ta disc at 760 μm distance from the Wehnelt aperture.

3.3. Energy resolution

The energy width of the electron pulses as a function of Wehnelt bias is shown in Fig. 7a and b. Here, spectra were taken without a specimen. At the minimum bias, the energy widths (FWHM) of more than 100 eV are much higher than what is usually obtained in thermionic emission (1–2 eV). Such a large energy distribution suggests that strong electron-electron interactions occur, resulting from space charge around the cathode and the Boersch effect in the beam cross-overs [2]. In all configurations, the energy width decreases with increasing bias. Several contributions have to be considered. At higher bias and lower electron energies, the cross-over is reached close to the Wehnelt so that a broader ΔE would be expected. On the other hand, the convergence angle at high bias is larger, leading to electron-electron interaction only along a short distance on the optical axis and thus giving a shorter interaction time. If the electrons are already "thermalized" in the cross-over, the longitudinal Boersch effect saturates and no further increase in energy width occurs at increasing current [23]. At low bias (which is still enough to weakly focus the beam at the anode), the beam is well collimated, such that electrons spend a longer time close together and repelling each other. At high bias, the beam is strongly focused and then rapidly expanded such that the Coulomb repulsion will be only occur for a brief moment and quickly attenuates, resulting in less energy spread at the end of gun.

An alternative explanation for the decrease in energy spread may be the influence of the chromatic aberrations of the Wehnelt that acts as a crude energy filter, provided the energy spread is due to space charge on the cathode. Chromatic aberrations of the Wehnelt would have an especially strong effect at large energy distributions that occur, e.g., within the shank emission ring as shown in Fig. 7c. Here, the more energetic electrons stem from the inner and the less energetic electrons from the outer areas of the ring. Hence, the narrowing of the energy distribution can be attributed to energy filtering by the Wehnelt that only transmits electrons of narrow energy range while electrons of differing energies are spread and omitted by one of the anode apertures in the accelerator. As the bias increases, the Wehnelt crossover gets closer to the cathode, the aberration and the energy dispersion increase, and more photoelectrons are filtered.

In Fig. 7b, the evolution of ΔE as a function of bias is measured for the shank emission and the on-axis electrons separately (Ta tip with a 550 μm Wehnelt-cathode gap). The shank emission shows a similar evolution as in Fig. 7a, with a broad energy distribution at low bias which narrows as the bias increases. However, the on-axis electrons (central spot) have an energy width of only 2 eV at minimum bias, slowly increasing to 10 eV until the large ring vanishes and ΔE drops again. This can be related to the low number of on-axis electrons (less than 2 pA) as shown in Fig. 4d and only a slight increase in current with higher bias. Low currents lead to a smaller Boersch effect in the gun cross-over which keeps the energy distribution narrow.

Although energy broadening effects can be avoided by reducing the number of electrons in one pulse, realistic acquisition times normally require high UV intensities to generate a sufficient number of electrons to provide short exposure times. However, this is at the expense of space charge and increased Boersch effects. Fig. 8 shows the effect of UV intensity (proportional to the number of electrons in the pulse) on the energy and temporal width. The energy broadening (Fig. 8a) is (almost) linearly proportional to the UV intensity and more pronounced at low bias, due to the filtering effect described above. Interestingly, the effect of the UV power on the pulse length (Fig. 8b) is only moderate. This confirms the presence of repulsion effects and large energy widths of the pulses, both increasing with the number of electrons per pulse, which cannot be responsible for the major part of the temporal broadening. Instead, the extraction field on the cathode surface, the contribution of electrons on trajectories of different length, and filtering effects by the Wehnelt have to be responsible for the different behavior of ΔE and Δt with increasing number of electrons per pulse.

4. Discussion

The results of this parametric studies show how time resolution, signal intensity, and energy resolution can be optimized and traded-off for different experimental needs. One of the main results shows that despite their low intensity, on-axis electrons may have both small ΔE and Δt, thus providing the best conditions for ultrafast EELS. For both cathode types studied, aberration-induced halos have to be suppressed to reduce trajectory effects with large temporal spread (Fig. 9a). If conical tips are used, shank emission should be suppressed or separated.

At a UV power of 2 nJ/pulse, as used in most of the measurements of this study (a possible loss of UV power on the in-column mirror is not taken into account here), we obtain approximately 7×10^4 electrons per pulse by assuming a quantum efficiency of the Ta cathode of 2.5×10^{-5} (including the reflectivity) [24]. This is orders of magnitude above the single-electron level so that repulsion effects are unavoidable as evident from the measured

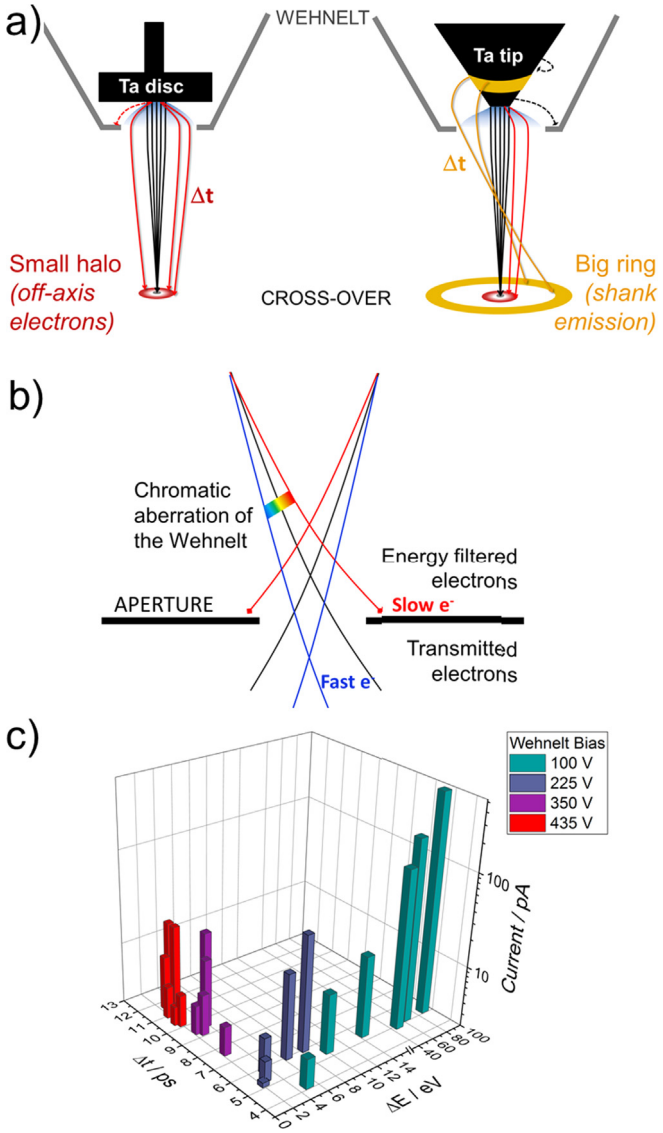

Fig. 9. (a) Schematic drawing of the different electron trajectories in the gun. (b) Filtering by an aperture via the chromatic aberration of the Wehnelt. (c) 3D plot presenting the evolution of the photoelectron current density as a function of pulse duration and energy width.

energy spreads (Fig. 7). Under suitable conditions, i.e. at high Wehnelt bias, ΔE can be reduced using the chromatic aberrations of the Wehnelt and the fixed apertures in the accelerator as an energy filter for the electron pulses (Fig. 9b). However, at high bias, electrons with trajectories of different lengths contribute to the beam which leads to an effective temporal broadening. In this configuration, narrow energy distribution, short pulses, and high current density cannot be combined and trade-offs must be made, based on the experimental requirements (Fig. 9c). A possible solution would be working at an intermediate bias where a halo appears in the filament image, so that the retarded electrons from the off-axis or shank emission (ring) can be excluded by apertures, though at the expense of intensity.

The Wehnelt bias affects space charge effects by modifying the electron emission area on the cathode and the early energy spread of the electrons (the higher the bias, the slower the electrons and the longer is the interaction time). It also has an influence on the Boersch effect by shifting the cross-over along the acceleration path and so along different electron energies and changing the convergence angle. The existence of long pulses is due to low extraction fields on the cathode and to the mixing of electron populations with different arrival times, which occurs when high bias and the double focusing of Wehnelt allows the collection of electrons from different angles with different path lengths and for them to be transmitted to the specimen.

Ta disc cathodes with 550 μm gap give a wide range of options. At low bias, we can obtain high signal and high temporal resolution at the cost of energy and spatial resolution. At high bias, we obtain high energy and high spatial resolutions but low temporal resolution and signal. The optimal gap for a flattened tip would be shorter than 550 μm to suppress the emission only at or above the highest bias voltage. However, this risks discharging problems due to the high extraction field at the cathode. A flat-tip cathode is preferred for high spatial resolution because the source emittance (of the flat area) is much smaller than on a disc, but the brightness of the beam would be similar.

We see that the largest contribution to the temporal spread is due to electrons propagating on different trajectories. Retarding effects and different lengths of trajectories determine the arrival time of the electrons on the specimen. High temporal resolution therefore needs the separation of trajectories and the selection of only those electrons with similar path lengths. Again, this can be achieved by using a bias voltage lower than one in which a small halo appears, e.g., below 600 V for a 550 μm Wehnelt-cathode gap. The large energy spread (from space charge effect) does not necessarily translate into a large temporal spread as has been shown above.

In a recent computational study [12], the beam parameters have been calculated for zero bias as a function of the tip-Wehnelt distance and size of the Wehnelt aperture. However, only two tip-Wehnelt distances, both larger than in the previous simulation, were used in this study and the Wehnelt aperture was not changed. Nevertheless, the large energy width simulated at zero bias [12] agrees quantitatively with our results. It has also been predicted that the energy width does not depend on the tip-Wehnelt distance which is also in accordance with our results for the tip (but not for the large area disc cathode). We see a larger temporal broadening than predicted in Ref. [12], which we attribute to having more electrons in the pulse in current study and to influence of trajectory effects on the broadening.

To find out whether cross-overs of the magnetic lenses in the microscope have an influence on the temporal and energy spread, all lenses of the UTEM were switched off, one after another, while ΔE was measured. No considerable influence was observed so that only the Wehnelt electrode affects the electron pulses. This is not unexpected since the charge density at these crossovers is much lower than at the gun crossover, and the electrons having an energy of 200 keV are moving fast enough to be in the cross-over regime for only fraction of the electron-electron mean scattering time [23]. Furthermore, by the time the beam has expanded to a few ps at 200 keV, its aspect ratio at a crossover with diameter in the micron range is more pencil-shaped than pancake-shaped, so homogeneous space charge effects may act to defocus the beam but will have almost no effect on pulse duration or energy spread [18].

Because of the chromatic aberration of the objective lens ($C_c = 1.4$ mm), a large ΔE of the order 100 eV deteriorates the spatial resolution but keeps it in the nanometer range. Under these conditions, the bright shank emission (giving even more current than a disc) can be used at low bias for very short acquisition times at 3 ps temporal resolution in order to probe dynamics occurring at this scale. This would be tolerable in imaging at lower magnification and in diffraction studies. For studies at high temporal resolution, the bias has to be finely tuned to avoid the contribution of halos from large-angle trajectories. A high ΔE is prohibitive for both high-resolution imaging and EELS, but acquiring an EEL spectrum does not always require high beam current. Hence, using

the central spot in a Ta tip configuration with 550 μm cathode-Wehnelt gap offers ideal conditions to combine high energy with high temporal resolution ($\Delta E = 1$ eV, $\Delta t = 2.5$ ps).

Better time resolutions, in the range of the UV laser pulse duration, have already been reported, i.e. as short as 300 fs in a similar setup [11]. However the better temporal resolution in previous results [11] were obtained using a sharp LaB_6 tip (6 μm radius) and at the lowest Wehnelt bias, i.e. where the extraction field on the tip is high and trajectory effects which drive the temporal broadening are negligible. Under the conditions similar to ours (300 V bias, 350 fs UV laser pulse), a pulse duration > 2 ps is reported in Ref. [11], which is in good agreement with our results.

5. Conclusions

As it is shown in this study, ultrafast TEM with a thermionic gun and adjustable Wehnelt bias offers many advantages in terms of flexibility with different applications. However, the gun parameters have to be tuned according to the application. Working in a quasi-single-electron regime is not feasible for many materials science investigations. If the single-electron criterion is applied to the cathode and assuming a typical transmission of 10% of the electrons to the detector, only every tenth pulse would send an electron, requiring exposure times of minutes to hours depending on the repetition rate. It is therefore necessary to be able to work with many electrons in one pulse and optimize the microscope settings to reduce the influence of space charge and Boersch effects by adjusting Wehnelt bias, cathode-Wehnelt gap, and the number of electrons per pulse.

The UV laser intensity and the number of electron per pulse should be set and maximized for the conditions of experiments such that effects from repulsion and resulting temporal and energy broadening effects are still within acceptable limits. The main influence of space charge and Boersch effects on the beam characteristics is the broadening of the energy profile of the electron pulses. However, this can be avoided by working at high Wehnelt bias. Energy filtering by the chromatic aberration of the Wehnelt allows the selection of an emission region with narrow energy spread. Our experiments suggest that the temporal width of the pulses is influenced by different electron trajectories in the gun. Selecting a certain trajectory and masking undesired shank emission or large-angle trajectories close to the Wehnelt aperture is possible at undersaturated Wehnelt settings. Maximizing all parameters at the same time is impossible with the configuration of standard thermionic guns, but a certain compromise between temporal and energy resolution as well as beam intensity and coherence can be found for most applications.

If intense pulses are needed for short exposure times, shank emission and large-angle trajectories can be collected to achieve shorter integration times. However, this is at the expense of energy and temporal resolution but may often be tolerable at lower-magnification imaging and diffraction. On the other hand, if only on-axis electrons are selected (which is possible due to the high flexibility of the Wehnelt setup), an energy resolution of better than 2 eV and a temporal resolution of better than 2 ps is achievable even when an order of 8000 electrons is in one pulse on the cathode level (of course, the number of electrons on the specimen is substantially reduced due to filtering effects of the Wehnelt at high bias).

It is quite obvious that an optimized design of the Wehnelt assembly would improve the characteristics of the pulses in terms of energy width and beam intensity. An optimized shape of the Wehnelt or an additional electrostatic lens could reduce the chromatic aberration. Together with an improved design of the cathode, more uniform electron trajectories could be achieved to reduce the temporal spread.

Although this study gives recipes for carrying out ultrafast TEM at different requirements, a detailed understanding of the variety of phenomena is still lacking. Extensive ray tracing simulations including electron-electron interaction within a pulse will be necessary to confirm the scenarios that are developed in this study. In a follow-up study, we will carry out detailed numerical simulations and analytical estimations to relate the experimental results to a refined model of pulse propagation. On the technical side, the development of new electron guns with improved emission parameters for pulsed TEM will also rely on both experimental and computational efforts.

Acknowledgements

Funding by the EQUIPEX program of the Agence Nationale de Recherche (France), contract ANR-11-EQPX-0041 (project UTEM) is gratefully acknowledged. We thank F. Carbone and B. J. Siwick for helpful discussions.

References

[1] H. Dömer, O. Bostanjoglo, High-speed transmission electron microscope, Rev. Sci. Instrum. 74 (2003) 4369–4372.
[2] W.E. King, G.H. Campbell, A. Frank, B. Reed, J.F. Schmerge, B.J. Siwick, B. C. Stuart, P.M. Weber, Ultrafast electron microscopy in materials science, biology, and chemistry, J. Appl. Phys. 97 (2005) 111101.
[3] J.S. Kim, T. LaGrange, B.W. Reed, M.L. Taheri, M.R. Armstrong, W.E. King, N. D. Browning, G.H. Campbell, Imaging of transient structures using nanosecond in situ TEM, Science 321 (2008) 1472–1475.
[4] B. Barwick, H.S. Park, O.-H. Kwon, J. Spencer Baskin, A.H. Zewail, 4D imaging of transient structures and morphologies in ultrafast electron microscopy, Science 322 (2008) 1227–1231.
[5] V.A. Lobastov, R. Srinivasan, A. Zewail, Four-dimensional ultrafast electron microscopy, Proc. Nat. Acad. Sci. USA 102 (2005) 7069–7073.
[6] H. Zewail, Four-dimensional electron microscopy, Science 328 (2010) 187–193.
[7] M.R. Armstrong, K. Boyden, N.D. Browning, G.H. Campbell, J.D. Colvin, W. J. DeHope, A.M. Frank, D.J. Gibson, F. Hartemann, J.S. Kim, W.E. King, T. B. LaGrange, B.J. Pyke, B.W. Reed, R.M. Shuttlesworth, B.C. Stuart, B.R. Torralv, Practical considerations for high spatial and temporal resolution dynamic transmission electron microscopy, Ultramicroscopy 107 (2007) 356–367.
[8] H.S. Park, J. Spencer Baskin, O.H. Kwon, A.H. Zewail, Atomic-scale imaging in real and energy space developed in ultrafast electron microscopy, Nano Lett. 7 (2007) 2545–2551.
[9] A. Gahlmann, S.T. Park, A.H. Zewail, Ultrashort electron pulses for diffraction, crystallography and microscopy: theoretical and experimental resolutions, Phys. Chem. Chem. Phys. 10 (2008) 2894–2909.
[10] F. Carbone, Modern electron microscopy resolved in space, energy and time, Eur. Phys. J. Appl. Phys. 54 (2011) 33503.
[11] L. Piazza, D.J. Masiel, T. LaGrange, B.W. Reed, B. Barwick, F. Carbone, Design and implementation of a fs-resolved transmission electron microscope based on thermionic gun technology, Chem. Phys. 423 (2013) 79–84.
[12] E. Kieft, K.B. Schliep, P.K. Suri, D.J. Flannigan, Effects of thermionic-gun parameters on operating modes in ultrafast electron microscopy, Struct. Dyn. 2 (2015) 051101.
[13] D.A. Plemmons, S.T. Park, A.H. Zewail, D.J. Flannigan, Characterization of fast photoelectron packets in weak and strong laser fields in ultrafast electron microscopy, Ultramicroscopy 146 (2014) 97–102.
[14] A. Feist, K.E. Echternkamp, J. Schauss, S.V. Yalunin, S. Schäfer, C. Ropers, Quantum coherent optical phase modulation in an ultrafast transmission electron microscope, Nature 521 (2015) 200–203.
[15] O.-H. Kwon, B. Barwick, H.S. Park, J. Spencer Baskin, A.H. Zewail, 4D visualisation of embryonic, structural crystallization by single-pulse microscopy, Proc. Nat. Acad. Sci. USA 105 (2008) 8519–8524.
[16] S.T. Park, M. Lin, A.H. Zewail, Photon-induced near-field electron microscopy (PINEM): theoretical and experimental, New J. Phys. 12 (2010) 123028.
[17] S.T. Park, O.-H. Kwon, A.H. Zewail, Chirped imaging pulses in four-dimensional electron microscopy: femtosecond pulsed hole burning, New J. Phys. 14 (2012) 053046.
[18] B.W. Reed, Femtosecond electron pulse propagation for ultrafast electron diffraction, J. Appl. Phys. 100 (2006) 034916.
[19] B.W. Reed, T. LaGrange, R.M. Shuttlesworth, D.J. Gibson, G.H. Campbell, N. D. Browning, Solving the accelerator-condenser coupling problem in a nanosecond dynamic transmission electron microscope, Rev. Sci. Instr. 81 (2010) 053706.

[20] L. Reimer, H. Kohl, Transmission Electron Microscopy, Fifth ed., Springer, Berlin, Heidelberg, New York, 2008.
[21] B. Barwick, D.J. Flannigan, A.H. Zewail, Photon-induced near-field electron microscopy, Nature 462 (2009) 902–906.
[22] M.E. Haine, P.A. Einstein, Characteristics of the hot cathode electron microscope gun, Br. J. Appl. Phys. 3 (1952) 40–46.
[23] H. Rose, R. Spehr, Energy broadening in high-density electron and ion beams: the Boersch effect, Adv. Electron. Electron Phys. 13 (Suppl. C) (1983) S475–S530.
[24] M. Cordona, L. Ley, Photoemission in solids, in: M. Cordona, L. Ley (Eds.), Topics in Applied Physics, 26, Springer-Verlag, New York, NY, 1978.